Microstructure evolution and improved surface properties of Ti-6Al-3Nb-2Zr-1Mo alloy by laser shot peening

GaoliLuo [a], Lingfeng Zhang [a,b,], Yi Xiong [a,b], Baofeng Zhang c, Xuepeng Chen [a], YongliWu [a], ShuboWang d, WeiCao [d]*

[a] *School of Materials Science and Engineering, Henan University of Science and Technology, Luoyang 471023, Henan, China*
[b] *Provincial and Ministerial Co-construction of Collaborative Innovation Center for Non-ferrous Metal New Materials and Advanced Processing Technology, Luoyang 471023, Henan, China*
[c] *School of Mechanical Engineering, Huanghe S&T University, Zhengzhou 450063, Henan, China*
[d] *Nano and Molecular Systems Research Unit, University of Oulu, FIN-90014, Finland*
** Corresponding author: zh_lingfeng@163.com.*

Abstract: In this work, the surface modification of Ti-6Al-3Nb-2Zr-1Mo (Ti80) alloy was performed by laser shock peening (LSP). The resultant microstructure, mechanical properties and corrosion properties of LSP-treated (LSPed) Ti80 were systematically investigated by 3D profiler, x-ray diffractometer (XRD), optical microscope (OM), transmission electron microscope (TEM), scanning electron microscope (SEM), microhardness tester, tensile tester and electrochemical workstation. LSP induced significant number of dislocations through plastic deformation, forming many defects such as dislocation tangles, stacking faults and deformation twins. The surface grain was severely refined due to severe plastic deformation at the surface. Microhardness improved substantially by 26.7%, compressive residual stress reached its maximum value (−307 MPa), and both microhardness and compressive residual stress presented a gradient change along

depth. The tensile properties were improved by the action of work hardening, grain refinement and compressive residual stresses after LSP. The fracture changed from typical ductile to mixed ductile and brittle fracture. Grain refinement provides more nucleation sites for the formation of passivation film, while impurities are not easily segregated at grain boundaries, retarding intergranular corrosion, high-density dislocations hinder electron transfer and reduce corrosion current density, resulting in a significant improvement in the corrosion resistance of Ti80 alloy in 3.5% NaCl and 5M HCL solution.

Keywords: laser shock peening, Ti-6Al-3Nb-2Zr-1Mo alloy, microstructure, mechanical properties, corrosion property

1. Introduction

Ti80 alloy, Ti-6Al-3Nb-2Zr-1Mo, is a new type of near-α-type high-temperature Ti alloy, which has greatly improved its overall performance of strength, toughness, weldability and corrosion resistance compared to traditional Ti alloys (Ref 1-2). Therefore, it has been widely used in pressure pipelines and structural parts subjected to relatively large loads in the marine environment, such as pressure hulls of bathyscaphs (Ref 3). However, high pressure and salinity of deep seawater can easily cause corrosion and premature failure of the parts due to surface damage of the materials (Ref 4). Hence, it is very momentous to ameliorate the mechanical and corrosion properties of such alloy to extend its service life.

Recently, studies on surface modification technologies, for instance, rotation accelerated shot peening (RASP) (Ref 5), ultrasonic shot peening (USP) (Ref 6), ultrasonic surface rolling (USR) (Ref 7), laser shock peening (LSP) (Ref 8), to improve the properties of Ti alloys have been intensively carried out. Compared with other surface treatment processes, for example, SP and rolling, laser shock peening (LSP) is a relatively novel surface modification technology and has the virtues of high strain rate, no thermal influence, no contact, precise controllability and no pollution (Ref 9,10,11). LSP employs a high power density and short pulse laser to irradiate the materials' surface. It generates a high-density plasma explosion, forming a shock wave and leading to plastic deformation of the surface layer. Therefore, deeper and larger amplitude of compressive residual stress field can be achieved without significantly increasing the surface roughness of the components (Ref 10,11,12,13), which significantly improves the mechanical and corrosion properties of materials (Ref 14). For example, Yang et al. (Ref 15) found that the LSPed TC17 alloy formed a gradient microstructure along depth. The increase in surface microhardness was ascribed to strengthening by grain refining and formation of high-density crystal defects. Zhou et al. (Ref 16) concluded that a single LSP increased the microhardness of TC6 alloy and formed a severe plastic deformation (SPD) layer, and increasing the duration of LSPs continuously increased the microhardness and the thickness of SPD layer. Yang et al. (Ref 17) concluded that the fretting fatigue life of LSPed TC11 alloy was mended, and the increase in laser power led to the nucleation sites of fatigue cracks moving from surface to interior the specimen. Shen et al. (Ref 18) proposed

that the grains of Ti-6Al-7Nb alloy were refined by multiple LSP. Therefore, the mechanical performances and wear resistance were improved, thereby extending the life of the components. The research results of Huang et al. (Ref 19) showed that the improved toughness of Ti-17 alloy was owing to the compressive residual stress and hardened surface layer induced by LSP. At the same time, the plasticity also increased with the appearance of deformation twins.

Previous investigations have mainly focused on the LSP treatment on traditional Ti alloys. However, there are few studies investigating the impact of LSP on the microstructure, mechanical and corrosion properties of Ti80 alloy. Hence, the microstructural evolution, mechanical and corrosion properties of Ti80 alloy treated by LSP were investigated in this work, hoping to broaden the surface treatment methods of Ti80 alloy to satisfy the property requirements of pressure hulls of bathyscaphs. This study is aimed at providing decisive insights for the enhancement of the pressure hulls of bathyscaphs surface structure and the application of key components of Ti80 alloy via LSP, bringing obvious social and economic benefits to the shipbuilding industry.

2. Material and experimental procedures

The forged Ti80 alloy bar was chosen for the experimental material, whose chemical composition is shown in Table 1.

Table 1 Chemical compositions of Ti80 alloy (wt.%)

Al	Nb	Mo	Zr	Fe	C	Si	H	O	N	Ti
5.8	3.0	1.1	1.9	0.10	0.05	0.08	0.008	0.10	0.04	Bal.

Before LSP, the Ti80 alloy bars were annealed in an artificial intelligence box-type resistance furnace (SGM) at 940 °C for 1.5 h and air cooling. The annealed Ti80 alloy bar was cut into the tensile specimens, whose geometry is schematically shown in Fig. 1. LSP (YS80-R200B) was performed on both sides of tensile specimens with a peened area of 6 × 25 mm^2 (black shade section in Fig. 1). It was mechanically ground and then fixed on a moving platform that can move freely in the X–Y direction, and LSP was made on both sides in turn. The processing parameters of LSP are listed in Table 2. The site experimental device diagram and schematic diagrams are shown in Fig. 2.

The 3D surface profiler was used to test the surface roughness of Ti80 alloys. The phase analysis was implemented by x-ray diffractometer (D8 ADVANCE), using Cu-Kα rays with an acceleration voltage of 40 kV, a step-scan speed of 2 °/min, step length of 0.02° and scanning range of 30-90°. The samples before and after LSP were mechanically ground and polished and then etched using a corrosive agent with V(HF):V(HNO_3):(H_2O) = 5:12:83. The metallographic microstructure was observed using an optical microscope (OLYMPUS PMG3). TEM foils were firstly prepared by mechanical grounding down to 50 μm. A ϕ3 mm disk was then punched out and thinned using Gatan 691 ion thinner. The microstructure was characterized via a JEM-2010 TEM operated at an electron acceleration voltage of 200 kV.

The microhardness of Ti80 alloy was tested employing a microhardness tester (MH-3). The depth distribution of microhardness was measured with a step of 20 μm

from the surface to matrix. At least 5 measurements were averaged as the resulting Hv value. Tensile tests were implemented using a tensile tester (Instron 5587) with a tensile speed of 0.5 mm/min. The characterization of fractures was carried out with JSM-IT200 scanning electron microscope with an electron acceleration voltage of 20 kV.

An electrochemical workstation (Autolab PGSTAT128N) was used for testing the corrosion behavior of Ti80 alloys before and after LSP. A conventional three-electrode cell system was employed in a 3.5% NaCl and 5M HCL electrolyte, respectively. Graphite electrode and saturated calomel electrode were employed as the auxiliary electrode and reference electrode, severally. The working electrode was a LSPed specimen with an exposed area of 1 cm^2 to electrolyte. Specimens were placed into electrolyte prior to tests to stabilize. Electrochemical impedance spectroscopy (EIS) and potentiodynamic polarization (PDP) were then measured sequentially. The EIS was performed between 10-2 Hz and 105 Hz using an excitation signal of 10 mV_{rms}, and the EIS data were fitted with ZsimpWin software. PDP was carried out from -0.65 $V_{vs.SCE}$ to 0.25 $V_{vs.SCE}$ at a scan rate of 0.001 V/s. The static immersion test was carried out at room temperature, and the corrosion rate was calculated using the loss of weight (Ref 20). The specimen was taken out every two days immersion, cleaned with acetone, alcohol, and distilled water successively to remove corrosion products, dried and weighed and then put into new solution for another 2 days. Each of the above experiments was repeated 3 times to ensure the reproducibility and accuracy of experimental data. The corrosion morphology was analyzed with

scanning electron microscope (JSM-IT200) with an electron acceleration voltage of 20 kV.

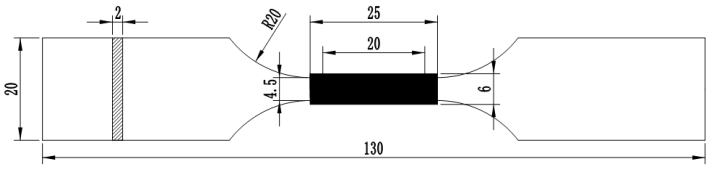

Fig. 1 Schematic of specimens employed for LSP (all dimensions are in mm).

Table 2 Processing parameters of LSP

Parameter	Value
Output beam divergence/mrad	≤2
Laser wavelength/nm	1064
Repetition rate/Hz	4
Pulse width/ns	20
Pulse energy/J	7
Spot diameter/mm	3
Overlapping rate/%	50
Pulse to pulse energy stability/%	＜1
Power density/(GW/cm^2)	4.95

3. Results

3.1 Surface roughness

The three-dimensional surface morphology of Ti80 alloy before and after LSP is displayed in Fig. 3. The surface is uniform and smooth before LSP (Fig. 3a). Some pits and protrusions appear after LSP (Fig. 3b). The measured surface roughness (Sa), before and after LSP, are 0.451 and 0.501, while peak-to-valley (PV) are 4.313 μm and 4.986 μm, respectively. This difference is owing to the development of micro-pits and wrinkles on the surface after LSP. During LSP, the lap rate of 50% was used, leading to extrusion deformation (Ref 21). Gaussian distribution of laser energy leads to a pressure distribution decreasing exponentially from the center outward, resulting

in higher level of plastic deformation in the center of the laser spot and then the formation of impact craters (Ref 22, 23).

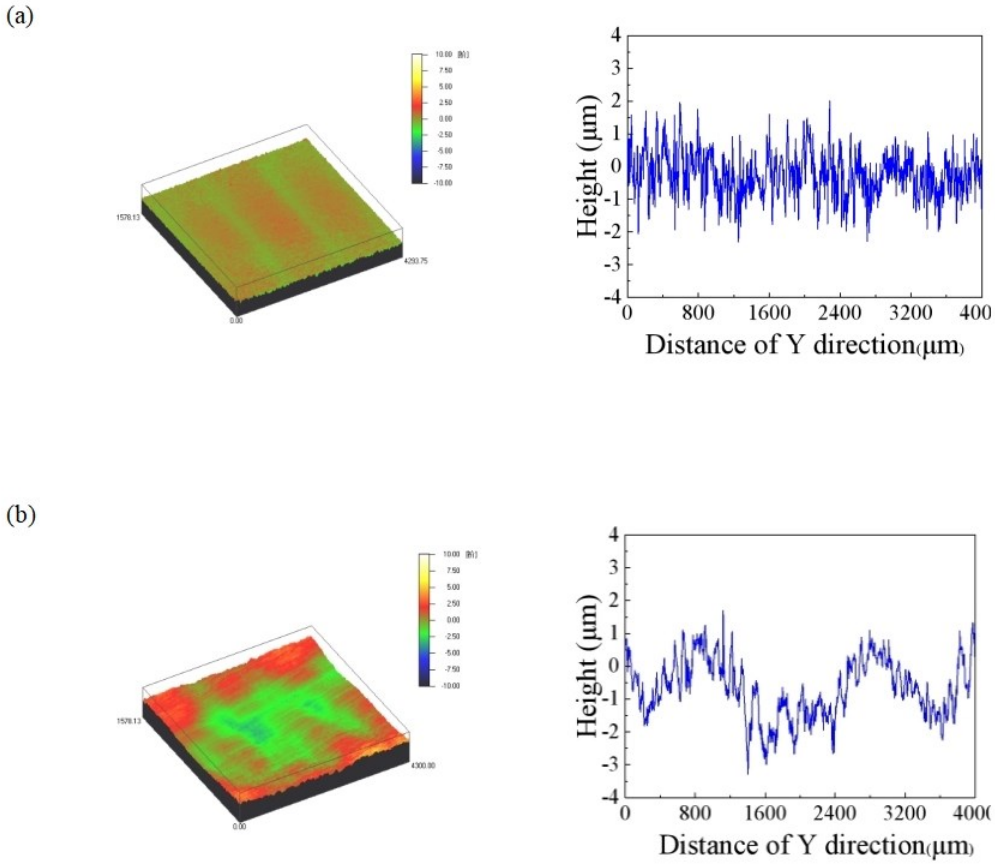

Fig. 2 Three-dimensional morphology and surface roughness of Ti80 alloy (a) before and (b) after LSP.

3.2 XRD analysis

Fig. 4 displays the XRD patterns of Ti80 alloys. Compared with the untreated sample, no new diffraction peak emerged in the XRD pattern after LSP, as shown in Fig. 4(a). However, the intensity of (110), $(10\bar{1}2)$, $(10\bar{1}3)$ and $(11\bar{2}1)$ diffraction peaks increased, indicating changes of texture after LSP (Ref. 24). The full width at half maximum (FWHM) of the diffraction peaks increase obviously (Fig. 4(b)), which is mostly contributed to grain refinement and the increase of surface microstrain after

LSP (Ref. 25). The microstrain and average grain size of the specimen surface of Ti80 alloy are evaluated by the Williamson–Hall (W–H) method (Ref 26, 27).

$$\beta \cos\theta = \varepsilon(4 \sin\theta) + K\lambda/D \qquad (1)$$

where, β is the FWHM of the diffraction peak, K is the constant ~ 0.9, λ is the X-ray wavelength, D is the average grain size, θ is the Bragg diffraction angle (in radians), and ε is the microstrain. The microstrain on the surface of the LSPed Ti80 alloy increase by 0.13%, and the average grain size is reduced to 23.1 nm. Furthermore, the $(11\bar{2}2)$, (110) and $(10\bar{1}1)$ peaks shift slightly after LSP. This is due to large compressive residual stresses generated on the Ti80 alloy surface under the action of high-energy shock waves during LSP, resulting in lattice distortion (Ref 28, 29).

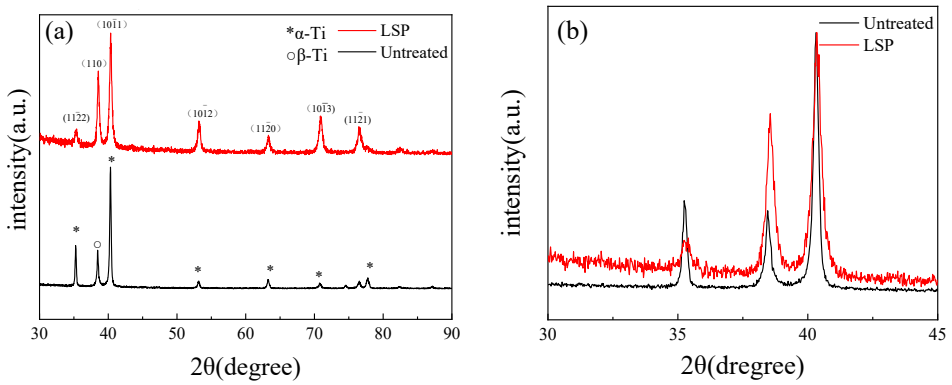

Fig. 3 XRD patterns of Ti80 alloy before and after LSP: (a) an overview with a range of 30-90°, and (b) magnified view with a range of 30-45°.

3.3 Microstructure evolution

Fig. 5(a) shows the microstructure of untreated Ti80 alloy. It exhibits a relatively coarse and equiaxial grain microstructure with primary α phase and a small quantity of transformation β (composed of secondary α and residual β). After LSP (Fig. 5b), the phase composition is still the primary α phase and a small amount of transformed

β, and the α phase grains are significantly smaller and more uniformly distributed compared to that before LSP. Figure 5(c), (d) shows the SEM images for the morphology of Ti80 alloy before and after LSP. The grain size of untreated Ti80 alloy is coarse (Fig. 5c), after LSP, the specimen surface appears SPD layer with the depth of about 81 μm (Fig. 5d), it can be seen that the grain boundary is not obvious and the grains are not easy to distinguish. The laser-induced peak pressure was evaluated as 2.2 GPa, according to the Fabbro model (Ref 30), and the HEL of Ti80 alloy is estimated as about 1.8 GPa by the Hugoniot elastic limit (HEL) model (Ref 31). Clearly, the peak pressure of the laser shock wave is higher than the HEL of Ti80 alloy, which causes the Ti80 alloy to undergo SPD, resulting in defects such as dislocations that increase in interior of the grains and eventually evolve into subgrain boundaries, which leads to grain refinement and improved surface uniformity.

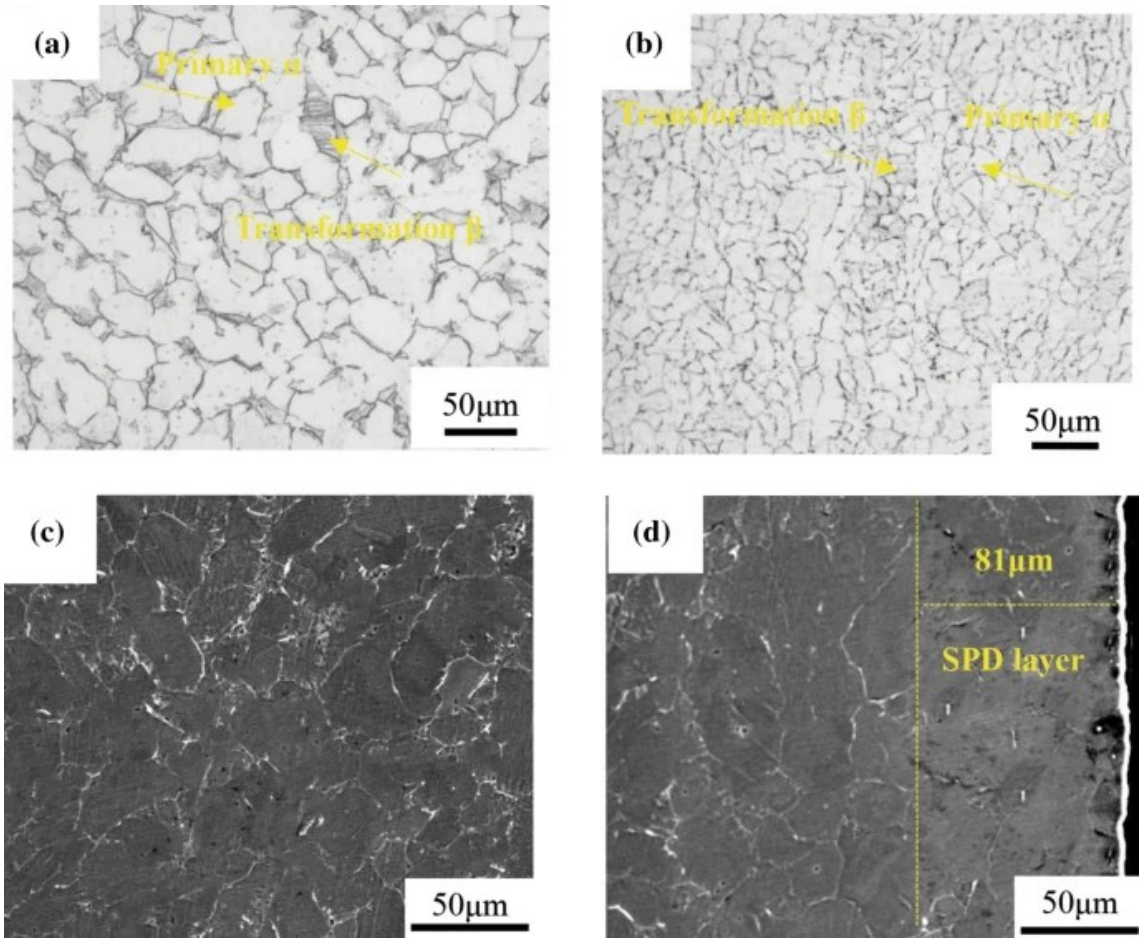

Fig. 4 Metallographic microstructure and SEM morphology of Ti80 alloy (a) Metallographic microstructure before and (b) after LSP, (c) SEM morphology before and (d) after LSP.

Fig. 6(a) shows that the typical equiaxial microstructure is obtained by annealing treatment, with the light lining for the α phase and the dark lining for the β phase, which corresponds to the microstructure in Fig. 5(a). Only a few dislocations and dislocation tangles are seen inside the α grains in Fig. 6(a)–(b). After LSP, a large number of dislocations, dislocation tangles (Fig. 7a), dislocation walls (Fig. 7b), dislocation cells (Fig. 7c) and other defects are seen in the surface. During LSP, high-energy shock wave loading acts on the surface of the Ti80 alloy, causing many dislocations to grow in the α matrix, leading to a fast increase in dislocation density. Meanwhile, the multidirectional loading generated by the shock wave changes the slip

direction of dislocations between and within the grains, so that the interaction between dislocations occurs not only in the same slip system but also between different slip systems (Ref 16), forming dislocation tangles (Fig. 7a). With continuous action of strain, the dislocations move and rearrange continuously, forming dislocation walls (Fig. 7b) and dislocation cells (Fig. 7c) that evolve into subgrain boundaries (Fig. 7d). This microstructural change in turn splits and refines the grains. In addition, it can be seen that there are stacking faults and high-density dislocation tangles interacting with deformation twins (Fig. 7e), in which twin plane is {0002} (Fig. 7f). The hcp α phase of Ti80 alloy has low stacking fault energy, and the dislocations are easy to decompose in the low stacking fault energy materials. This facilitates the dislocation decomposition under the action of laser shock waves, resulting in many stacking faults in the α matrix. Dislocations cross-slip difficultly after decomposition, and the dislocations movement is easily impeded, which hinders plastic deformation. In order to coordinate the plastic deformation, it is necessary to activate multiple slip systems, however, when the stress direction under the action of shock waves is not sufficient for the simultaneous activation of multiple slip systems, deformation twin may occur (Fig. 7f) (Ref 32). Deformation twin boundaries can be used as a source of dislocation emission, thereby providing more mobile dislocations and allowing plastic deformation to continue. The combined effect of the dislocation and twin splitting mechanisms results in the grain refinement of Ti80 alloy, as shown in 3.2.

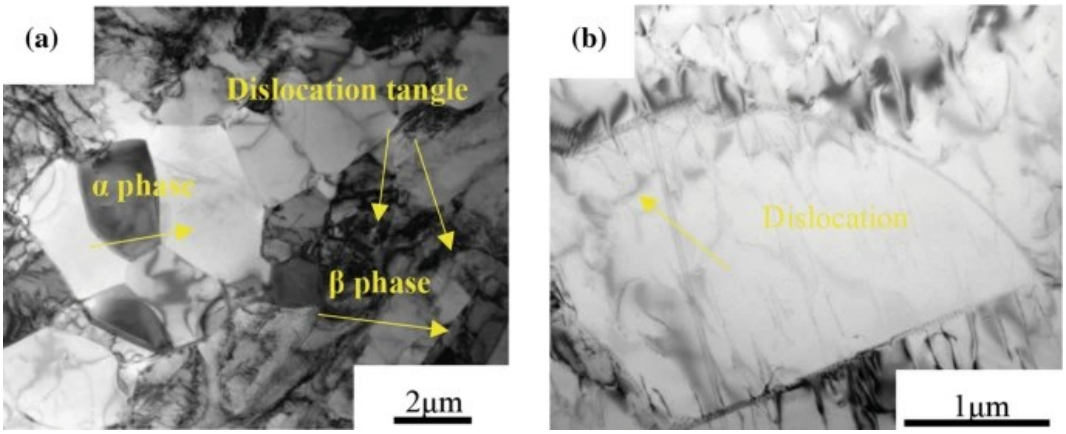

Fig. 5 TEM images of the surface Ti80 alloy before LSP

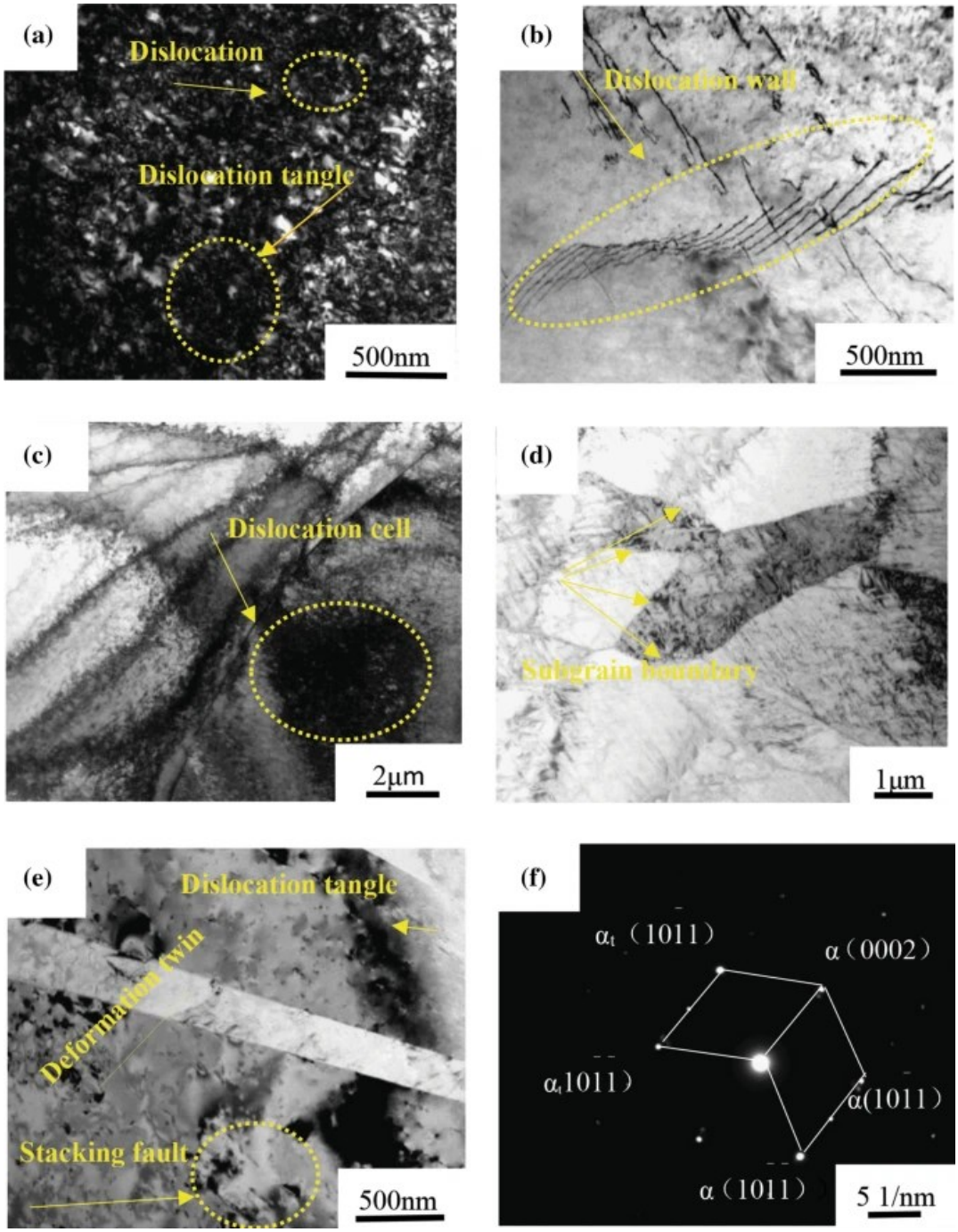

Fig. 7 Microstructure images of the surface Ti80 alloy after LSP.

3.4 Properties of Ti80 alloy before and after LSP

3.4.1 Microhardness

Fig. 8 displays the relationship between the microhardness of Ti80 alloy and the depth from the surface. As visible the microhardness value of the untreated Ti80 alloy is uniform, 270.9 HV. After LSP, the microhardness obviously increases to 343.3HV,

Improvement of the microhardness is the result of the strengthening effect of dislocations, deformation twins and other crystal defects introduced by plastic deformation and fine crystal strengthening (Ref 33).The microhardness of Ti80 alloy gradually decreases with the increase in layer depth, which is because the high-energy shock waves are generated on the surface during LSP, and it gradually attenuates with the increase in layer depth, and the degree of plastic deformation gradually decreases (Fig. 5d), resulting in the gradual weakening of the effects of work hardening and fine crystal strengthening, the microhardness value is gradually reduced to the matrix microhardness value, so that the microhardness presents gradient characteristic along depth.

Fig. 9 shows residual stress of Ti80 alloy with different layer depths before and after LSP. The surface of the untreated specimen introduced a smaller tensile residual stress of about 8 MPa due to the machining effect. After LSP, the compressive residual stress in the surface layer of Ti80 alloy reached −307 MPa, and the compressive residual stress layer depth was 175 μm. Due to the action of laser shock wave, the surface layer of Ti80 alloy undergoes severe plastic deformation, the region of severe plastic deformation is limited by the surrounding matrix without plastic deformation, resulting in the development of compressive residual stress field with a certain depth on the surface of the Ti80 alloy according to the principle of reaction of mechanical effects (Ref 34). At the same time, the laser shock wave will gradually decay with the increase in the layer depth, and the degree of plastic deformation gradually decreases, so the distribution of the compressive residual stress shows

gradient change characteristics with the change of the layer depth.

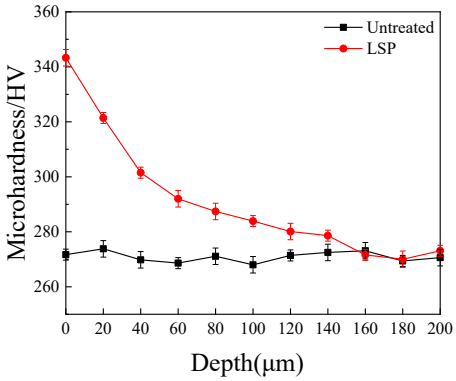

Fig. 8 Microhardness vs depth distribution of Ti80 alloy before and after LSP.

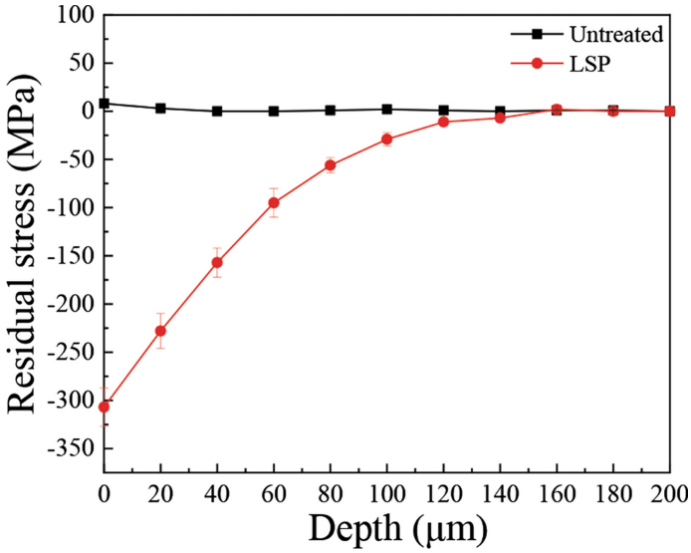

Fig. 9 Residual stress of Ti80 alloy with different layer depths before and after LSP.

3.4.2 Tensile properties

Fig. 10 shows the tensile properties of Ti80 alloy before and after LSP. The tensile strength, yield strength and elongation of the untreated Ti80 alloy are 730 MPa, 594 MPa and 15.5%. The tensile strength, yield strength and elongation of LSPed Ti80 alloy reach about 788 MPa, 637 MPa and 15.9%, respectively. The surface of LSPed Ti80 alloy undergoes severe plastic deformation, produces high-density dislocations, refines grains and then reduces the mean free path of the dislocation,

while crystal defects such as dislocation tangles and deformation twins are formed on the surface, the interaction of dislocations and twin boundaries can also reduce the mean free path of the dislocation, From Eq (2) in the literature (Ref 35), it follows that the tensile strength and yield strength of Ti80 alloy are significantly improved. Cracks are generated during tensile and the compressive residual stress reduces the rate of crack expansion while causing a crack closure effect, thus extending the crack expansion life (Ref 36). With a high tensile strain during the tensile process, the LSP-refined surface grains deform more uniformly and suppress strain concentration, resulting in increased plasticity. Simultaneously, the twin boundaries can act as dislocation emission sourced, thereby providing more mobile dislocation which can sustain the plastic deformation during tensile and ameliorate the elongation of the Ti80 alloy (Ref 37). With the combined effect of these factors, a good strength–plasticity match was obtained of LSPed Ti80 alloy.

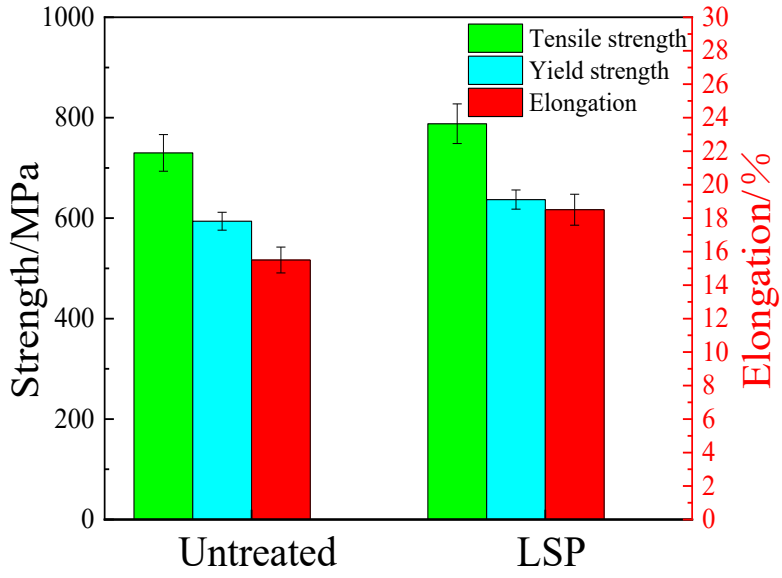

Fig. 10 Tensile properties of Ti80 alloy before and after LSP.

3.4.3 Tensile fracture morphology

Fig. 11(a) exhibits that the fracture morphology of the untreated Ti80 alloy is densely covered with dimples of 5 μm, showing obvious ductile fracture characteristics. The fracture morphology of the LSPed specimen shows mixed fracture characteristics of quasi-cleavage and ductile (Fig. 11b). The quasi-cleavage fracture appears in the SPD layer at the specimen surface with the depth of about 54 μm, meanwhile, a small amount of dimples are seen in the SPD layer, while many dimples appear in the matrix. The reason for this phenomenon is that the surface grains of LSPed Ti80 alloy are refined, inhibiting dislocation slip under the tensile stress. Only grain rotation and grain boundary movement occur, and plastic deformation is incomplete, thus the surface fracture morphology changes to quasi-cleavage fracture. While the internal coarse grain microstructure has good plastic deformation ability and still presents ductile fracture characteristics.

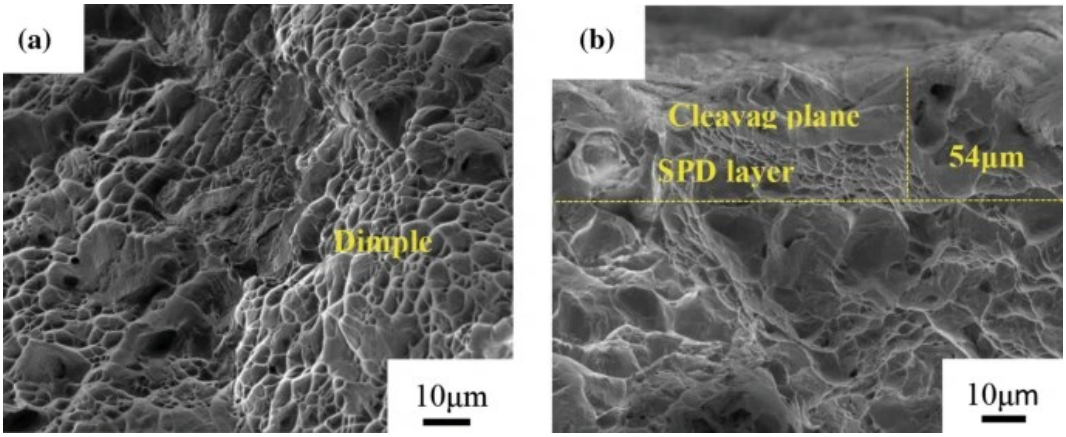

Fig. 11 Tensile fracture images of Ti80 alloy (a) before (b) and after LSP.

3.4.4 Corrosion properties

Fig. 12 shows the PDP curves of Ti80 alloys. The corrosion potential and corrosion current density were obtained by the Tafel extrapolation method. In 3.5 wt.% NaCl solution (Fig. 12a), the specimens exhibit similar electrochemical

behavior in the cathode branch. In all anodic branch, the specimens go directly to the passivation zone. In 5M HCL solution (Fig. 12b), there is a transition from activation to passivation in the anodic branch. The corrosion current density of Ti80 alloy increases rapidly with the increase in the corrosion potential, which is owing to the destruction of the original passivation film and the active dissolution of Ti80 alloy, which is also the beginning of the formation of corrosion pits (Ref 38). When the corrosion potential reaches a critical value, the surface of Ti80 alloy starts to passivate, and the corrosion current density gradually enters the stable zone. This is because the new passivation film formed has a protective effect. When the formation and destruction of the passivation film reach a balance, the current density will enter a steady state. Table 3 displays that the corrosion potential of the LSPed specimens in 3.5% NaCl solution shifts by 34.4 $mV_{vs.SCE}$ and the corrosion current density decreases by 21 $nA \cdot cm^{-2}$ compared to those of the untreated specimens. Similarly, the corrosion potential of the LSPed specimens in 5M HCL solution was positively shifted by 68.8 $mV_{vs.SCE}$ and the corrosion current density reduces by 0.9 $\mu A \cdot cm^{-2}$ compared to those of the untreated specimens. This positive shift of corrosion potential indicates that the thermodynamic stability of Ti80 alloy is enhanced by LSP. Meanwhile, the lower corrosion current density indicates that the LSPed Ti80 alloy is easier to passivate and the stability of the passivation film is good. Therefore, the above results show that the anticorrosion of LSPed Ti80 alloy in both 3.5% NaCl and 5M HCL solution is improved.

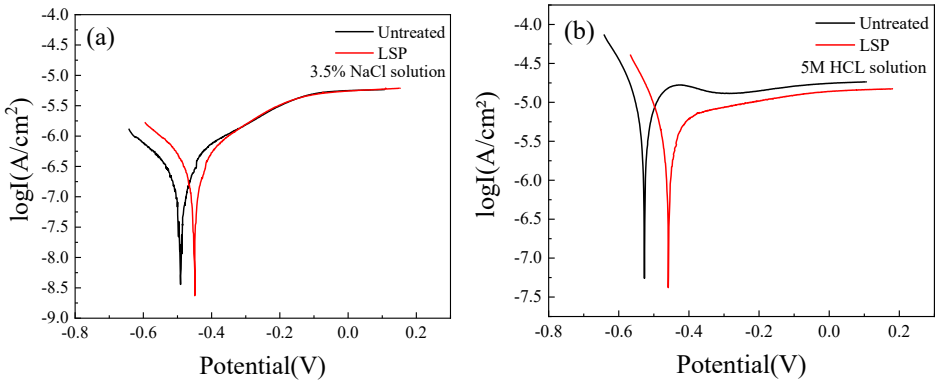

Fig. 12 PDP curves of Ti80 alloys in (a) 3.5 wt.% NaCl solution, and in (b) 5M HCl solution.

Table 3 Corrosion potential and Corrosion current density of Ti80 alloys

Electrolyte	Specimen	Corrosion potential ($mV_{vs.SCE}$)	Corrosion current density($\mu A \cdot cm^{-2}$)
3.5%NaCl	Untreated	-422.5±9	0.068±0.003
	LSP	-388.2±12	0.020±0.005
5MHCL	Untreated	-526.7±14	3.80±0.009
	LSP	-457.9±17	2.96±0.007

Figure 13 shows the EIS spectra of Ti80 alloys in 3.5% NaCl solution and 5M HCL solution. Nyquist plots of the samples exhibit a single capacitive loop. In both electrolytes, the radius of the capacitive loops of the LSPed Ti80 alloy is larger than those of the untreated one, suggesting the impedance of the LSPed Ti80 alloy increase (Ref 39). Correspondingly, the Bode plots (Fig. 13b, c, f, g) characterization shows that the phase and impedance of the Ti80 alloy before and after LSP remain constant and tend to zero in the high frequency range (10^5-10^3), indicating that the resistive properties of the electrolytes are ignorable. In the low frequency range (10^{-1}-10), the impedance of Ti80 alloy shows a rapid increase with decreasing frequency, indicating that the passivation film formed on the surface of the specimen has excellent

anticorrosion (Ref 38). The impedance values of LSPed Ti80 alloy are larger than those of the untreated specimens at the termination frequency, demonstrating that the anticorrosion of the LSPed Ti80 alloy in 3.5% NaCl solution and 5M HCL solution was ameliorated, which corresponds with the polarization test outcome.

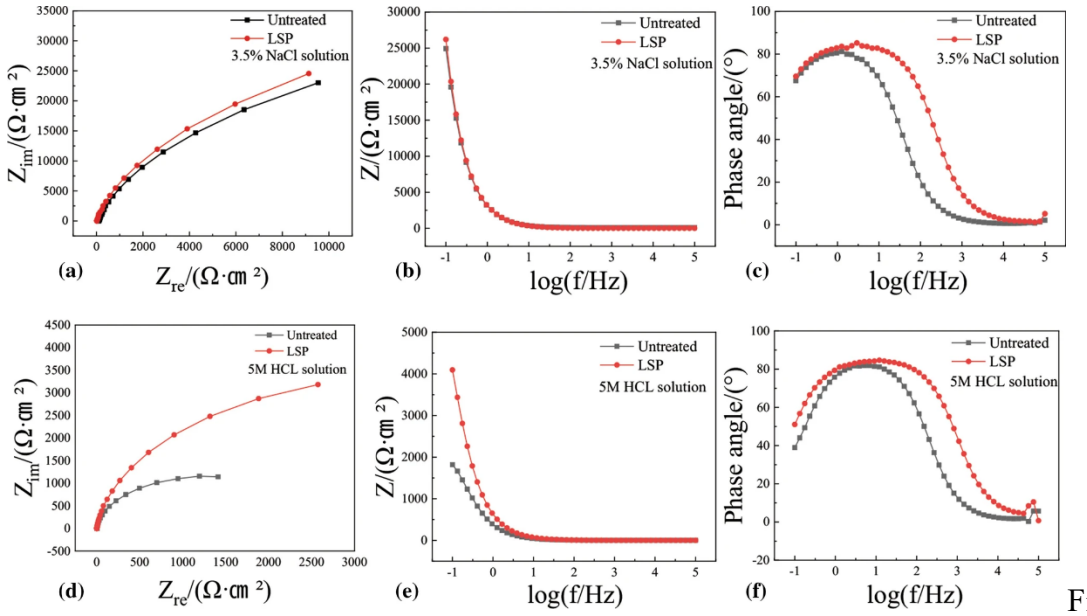

Fig

Fig. 13 EIS of Ti80 alloy before and after LSP in 3.5% NaCl solution and 5M HCL solution. (a,e) Nyquist plots, (b,f) Bode magnitude plots, (c,g) Bode phase plots.

To better investigate the corrosion behavior of Ti80 alloy, static immersion testing was conducted. Fig. 14(a), (b) shows the cumulative weight loss of the specimens with immersion time under different conditions. After ten days of immersion in 3.5% NaCl solution, the cumulative weight loss of the untreated specimens was 0.8 mg/cm^{-2} and the cumulative weight loss of the LSPed specimens was 0.6 mg/cm^{-2}, after ten days of immersion in 5M HCL solution, the cumulative weight loss of the untreated specimens was 5.2 mg/cm^{-2} and the cumulative weight loss of the LSPed specimens was 3.9 mg/cm^{-2},demonstrating that the anticorrosion of Ti80 alloy can be ameliorated by LSP. The corrosion rate I is evaluated according to (Ref 20):

$$I = KW/ATρ \quad (2)$$

where K is constant (8.76×10^4), W is the weight loss (g), A is soaked area (cm^2), T is immersion time (h), ρ is the density of the specimen (g/cm^3). In this case, A is 1 cm^2, T is 240 h, and ρ is 4.51g/cm^3. As shown in Fig. 14(c), (d), the corrosion rates of Ti80 alloy before and after LSP were calculated as 0.06 and 0.05 ($mm\cdot year^{-1}$), in 3.5% NaCl solution, 0.42 and 0.32 ($mm\cdot year^{-1}$) in 5M HCl, severally. The decreased corrosion rates provide a definite indicator for the retard corrosion of Ti80 alloy by LSP. This is owing to the presence of refined grains and increased fraction of grain boundaries provides more nucleation sites for passivation film (Ref 40). Meanwhile, compressive residual stress increases the lateral pressure stress of the passivation film, so that the density of the passivation film increases and is less prone to damage. Hence, the corrosion resistance of the material is improved (Ref 41-42).

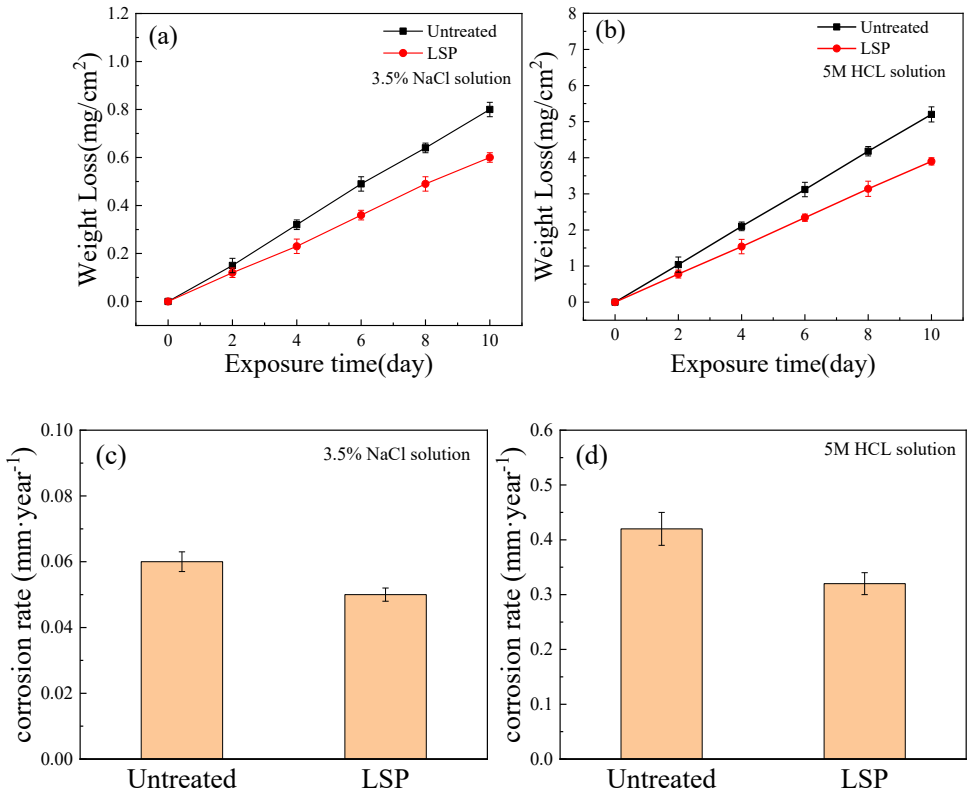

Fig. 14 Variation in loss of weight with time and corrosion rate of Ti80 alloy in (a,c) 3.5% NaCl solution and in (b,d) 5M HCl solution before and after LSP.

Fig. 15 displays the representative corrosion profiles of the Ti80 alloy after immersing in 3.5% NaCl solution (Fig. 15a–d) and in 5M HCL solution (Fig. 15e–h) for ten days. The corrosion cracks of LSPed specimen are smaller than those of the untreated specimen in 3.5% NaCl solution. Intergranular corrosion and numerous corrosion pits are identified for the untreated specimen in 5M HCL solution (Fig. 15e). It can be seen from the magnified view of the region A (Fig. 15f) that α phase is more prone to corrosion as compared with β phase. It is due to the uneven distribution of alloying elements in α and β phases which result in a lower chemical potential of the α phase than that of β phase, the α phase, therefore, is corroded preferentially (Ref 43). Intergranular corrosion is clearly identified on the corrosion profile of the LSPed specimen (Fig. 15g). No corrosion pits are found in Fig. 15(h) which is an enlarged view of region B in Fig. 15(g), suggesting an increase in the anticorrosion of LSPed Ti80 alloy. On the one hand, the grains Ti80 alloy before LSP is coarse, and impurities are more likely to deviate at grain boundaries thus causing intergranular corrosion, which is serious enough to form corrosion pit, thereby accelerating the corrosion rate of the alloy. On the other hand, LSP-induced grain refinement and high-density dislocations may also hinder corrosion pit diffusion (Ref 44). Hence, the anticorrosion of LSPed Ti80 alloy in both 3.5% NaCl and 5M HCL solution is improved.

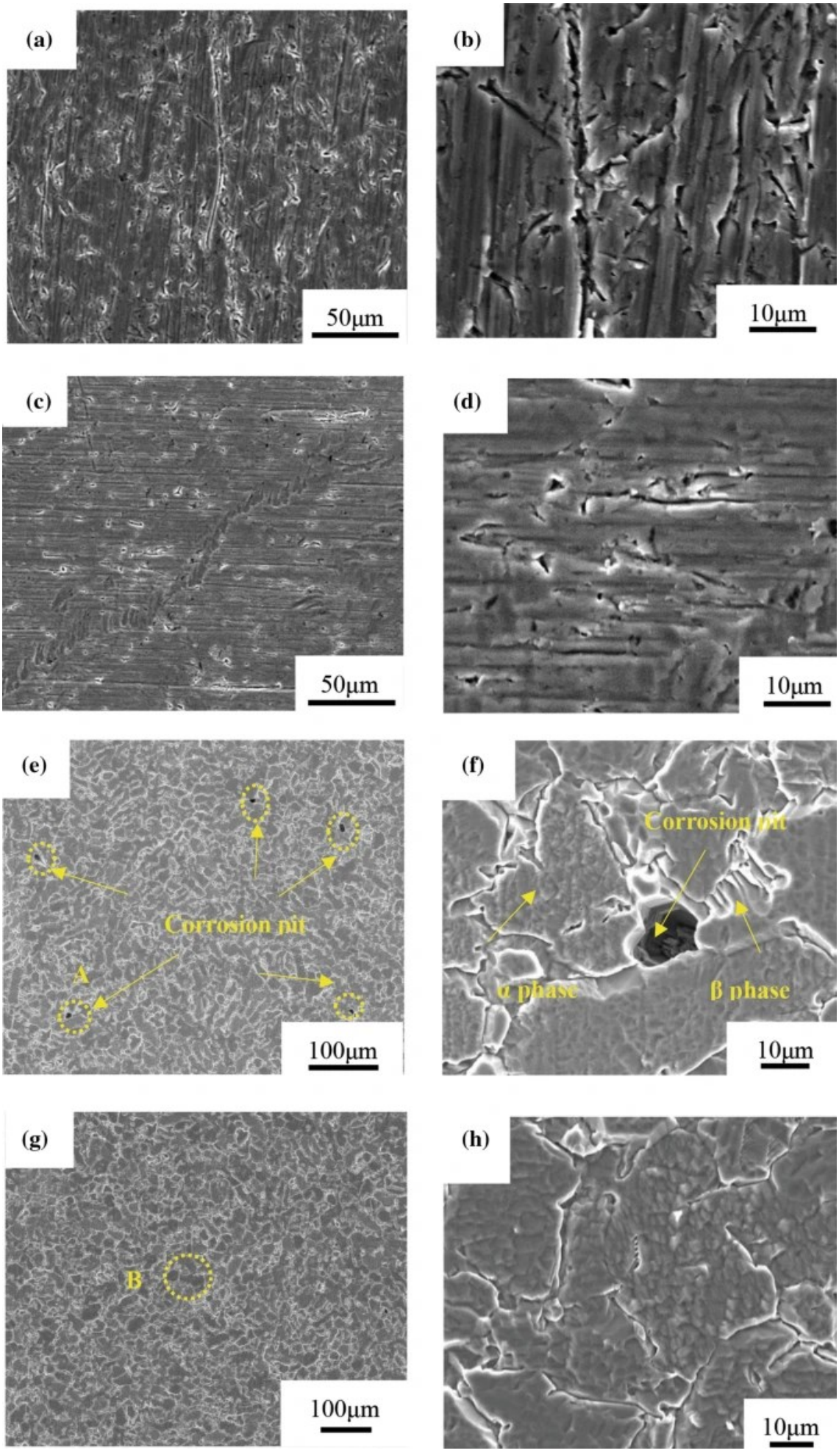
(a)
50μm
(b)
10μm
(c)
50μm
(d)
10μm
(e)
Corrosion pit
A
100μm
(f)
Corrosion pit
α phase
β phase
10μm
(g)
B
100μm
(h)
10μm

Fig. 15 Surface corrosion profiles of Ti80 alloy in 3.5% NaCl solution and in 5MHCl solution. (a–b) Corrosion profiles of Ti80 alloy before LSP in 3.5% NaCl solution, (c–d) corrosion profiles of LSPed Ti80 alloy in 3.5% NaCl solution, (e–f) corrosion profiles of Ti80 alloy before LSP in 5M HCL solution and (g–h) corrosion profiles of LSPed Ti80 alloy in 5M HCL solution.

4 Conclusion

In this study, LSP surface treatment of Ti80 alloy was implemented, and corresponding microstructure evolution and properties of Ti80 alloy were studied systematically. The main results can be drawn from the work:

(1) After LSP, many defects such as dislocation tangles, stacking faults and deformation twins were formed in the surface microstructure of Ti80 alloy, resulting in significant grain refinement.

(2) The strengthening effect of crystal defects combined with fine grain strengthening increased the surface microhardness by 26.7%, while a large compressive residual stress was formed, resulting in increased strength and elongation, the overall mechanical properties became better. The strength and elongation of Ti80 alloy increased by LSP, and the microhardness also increased significantly and showed a gradient change characteristic along the depth of the layer. The overall mechanical properties became better.

(3) The fracture morphology of Ti80 alloy changes from typical ductile fracture before LSP to mixed ductile and brittle fracture after LSP because the surface refined grains inhibit dislocation slip under the effect of tensile stress, and plastic deformation is incomplete.

(4) Grain refinement provided more nucleation sites for the formation of

passivation film of Ti80 alloy, while the compressive residual stress made the passivation film more dense and less susceptible to destruction, thus making the corrosion potential of Ti80 alloy in 3.5% NaCl and 5M HCL solution positively shifted, the corrosion current density was reduced, the corrosion rate was reduced, and the corrosion resistance was improved.

Acknowledgments

The authors want to thank the assistance from the National Natural Science Foundation of China (Grant Numbers U1804146 and 52111530068).

Conflict of interest

None.

References

[1] H.S. Chen, X.H. Liu, G.F. Liu, X.D. Tang, J.H. Luo, Y. Feng, J.S. Li and H.Z. Fu, Hot Deformation Behavior and Processing Map of Ti-6Al-3Nb-2Zr-1Mo Titanium Alloy, Rare. Metal. Mat. Eng., 2016, 45(4), p 901–906.

[2] S.J. Quan, K.X. Song, B.B. Zhang, Q. Wang, K.H. Zheng and D.D. Zhang, Effect of Heat Treatment Process on Microstructure of Ti80 Alloy, T. Mate. Heat. Treat, 2018, 39(5), p 44–52.

[3] Y.Q. Zhao, The New Main Titanium Alloy Used for Shipbuilding Developed in China and Their Applications, Mater. China, 2014, 33(07), p 398–404.

[4] B.X. Su, B.B. Wang, L.S. Luo, L. Wang, Y.Q. Su, F.X. Wang, Y.J. Xu, B.S. Han, H.G. Huang, J.J. Guo and H.Z. Fu, The Corrosion Behavior of Ti-6Al-3Nb-2Zr-1Mo Alloy: Effects of HCl Concentration and Temperature, J. Mater. Sci. Technol., 2021, 74(15), p 143–154.

[5] X.K. Ma, Z. Chen, D.L. Zhong, S.N. Luo, L. Xiao, W.J. Lu and S.L. Zhang, Effect of Rotationally Accelerated Shot Peening on the Microstructure and Mechanical Behavior of a Metastable β Titanium Alloy, J. Mater. Sci. Technol., 2021, 75, p 27–38.

[6] S. Kumar, K. Chattopadhyay, S.R. Singh and V. Singh, Surface Nanostructuring of Ti-6Al-4V Alloy Through Ultrasonic Shot Peening, Int. J. Sur. Sci. Eng., 2017, 11(1), p 23–35.

[7] Z.J. Ren, F.Q. Lai, S.G. Qu, Y.L. Zhang, X.Q. Li and C. Yang, Effect of Ultrasonic Surface Rolling on Surface Layer Properties and Fretting Wear Properties of Titanium Alloy Ti5Al4Mo6V2Nb1Fe, Surf. Coat. Tech., 2020,

389, p 125612.
[8] X.D. Ren, W.F. Zhou, F.F. Liu, Y.P. Ren, S.Q. Yuan, N.F. Ren, S.D. Xu and T. Yang, Microstructure Evolution and Grain Refinement of Ti-6Al-4V Alloy by Laser Shock Processing, App. Surf. Sci., 2016, 363, p 44–49.
[9] C.Y. Zhang, Y.L. Dong and C. Ye, Recent Developments and Novel Applications of Laser Shock Peening: A Review, Adv. Eng. Mater., 2021, 23(7), p 2001216.
[10] A. Chattopadhyay, G. Muvvala, S. Sarkar, V. Racherla and A.K. Nath, Effect of Laser Shock Peening on Microstructural, Mechanical and Corrosion Properties of Laser Beam Welded Commercially Pure Titanium, Opt. Laser Technol., 2021, 133, p 106527.
[11] Z.R. He, Y.Z. Shen, J. Tao, H.F. Chen, X.F. Zeng, X. Huang and A.A. El-Aty, Laser Shock Peening Regulating Aluminum Alloy Surface Residual Stresses for Enhancing the Mechanical Properties: Roles of Shock Number and Energy, Surf. Coat. Tech., 2021, 421, p 127481.
[12] L. Lan, R.Y. Xin, X.Y. Jin, S. Guo, B. He, Y.H. Rong and N. Min, Effects of Laser Shock Peening on Microstructure and Properties of Ti–6Al–4V Titanium Alloy Fabricated Via Selective Laser Melting, Mater., 2020, 13(15), p 3261.
[13] M. Abeens, R. Muruganandhan and K. Thirumavalavan, Effect of Low Energy Laser Shock Peening on Plastic Deformation, Wettability and Corrosion Resistance of Aluminum Alloy 7075 T651, Optik, 2020, 219, p 165045.
[14] A. Chattopadhyay, G. Muvvala, S. Sarkar, V. Racherla and A.K. Nath, Effect of Laser Shock Peening on Microstructural, Mechanical and Corrosion Properties of Laser Beam Welded Commercially Pure Titanium, Opt. Laser Technol., 2021, 133, p 106521.
[15] Y. Yang, H. Zhang and H.C. Qiao, Microstructure Characteristics and Formation Mechanism of TC17 Titanium Alloy Induced by Laser Shock Processing, J. Alloy Compd., 2017, 722, p 509–516.
[16] L.C. Zhou, Y.H. Li, W.F. He, G.Y. He, X.F. Nie, D.L. Chen, Z.L. Lai and Z.B. An, Deforming TC6 Titanium Alloys at Ultrahigh Strain Rates During Multiple Laser Shock Peening, Mat. Sci. Eng. A, 2013, 578, p 181–186.
[17] X.F. Yang, H.J. Zhang, H.T. Cui and C.L. Wen, Effect of Laser Shock Peening on Fretting Fatigue Life of TC11 Titanium Alloy, Mater., 2020, 13(21), p 4711.
[18] X.J. Shen, P. Shukla, S. Nath and J. Lawrence, Improvement in Mechanical Properties of Titanium Alloy (Ti-6Al-7Nb) Subject to Multiple Laser Shock Peening, Surf. Coat. Tech., 2017, 327, p 101–109.
[19] S. Huang, Y. Zhu, W. Guo, P. Peng and X.G. Diao, Impact Toughness and Microstructural Response of Ti-17 Titanium Alloy Subjected to Laser Shock Peening, Surf. Coat. Tech., 2017, 327, p 32–41.
[20] B.X. Su, L.S. Luo, B.B. Wang, Y.Q. Su, L. Wang, R.O. Ritchie, E.Y. Guo, T. Li, H.M. Yang, H.G. Huang, J.J. Guo and H.Z. Fu, Annealed Microstructure

Dependent Corrosion Behavior of Ti-6Al-3Nb-2Zr-1Mo Alloy, J. Mater. Sci. Technol., 2021, 62(03), p 234–248.
[21] Y.P. Yang, X.X. Chen, Y. Zhang and W.W. Zhang, Experimental Study on Mechanical Properties of AZ91D Magnesium Alloy by Laser Shock Peening, Appl. Laser, 2018, 38(05), p 798–804.
[22] Q.Y. Jiao, P.P. Han, Y. Lu, D. Zhao, H.C. Qiao and J.B. Zhao, Effect of Laser Shock Peening on Residual Stress and Mechanical Properties of TA15 Titanium Alloy, J. Plast. Eng., 2021, 28(03), p 146–152.
[23] R.J. Sun, L.H. Sun, Y. Zhu, P. Peng, L.X. Zhang and W. Guo, Effect of Laser Shock Peening on Microstructure and Tensile Properties of TC17 Titanium Alloy, Rare Metal. Mat. Eng., 2019, 48(02), p 491–499.
[24] X.L. Pan, X.D. Wang, Z. Tian, W.F. He, X.S. Shi, P.M. Chen and L.C. Zhou, Effect of Dynamic Recrystallization on Texture Orientation and Grain Refinement of Ti6Al4V Titanium Alloy Subjected to Laser Shock Peening, J. Alloy Compd., 2021, 850, p 156672.
[25] M. Kheradmandfard, S.F. Kashani-Bozorg, K.-H. Kang, O.V. Penkov, A.Z. Hanzaki, Y.-S. Pyoun, A. Amanov and D.-E. Kim, Simultaneous Grain Refinement and Nanoscale Spinodal Decomposition of β Phase in Ti-Nb-Ta-Zr Alloy Induced by Ultrasonic Mechanical Impacts, J. Alloy Compd., 2018, 738, p 540–549.
[26] S. Brandstetter, P.M. Derlet, S. Van Petegem and H. Van Swygenhoven, Williamson-Hall Anisotropy in Nanocrystalline Metals: X-ray Diffraction Experiments and Atomistic Simulations, Acta. Mater., 2007, 56(2), p 165–176.
[27] J. Markmann, V. Yamakov and J. Weissmüller, Validating Grain Size Analysis from X-ray Line Broadening: A Virtual Experiment, Scripta. Mater., 2008, 9(1), p 15–18.
[28] R. Sundar, C. Sudha, A.K. Rai, P. Ganesh, A. Kolhatkar, S. Murugesan, V. Karthik, R. Biswal, S. Raju, K. Ranganathan, R. Kaul and K.S. Bindra, Effect of Laser Shock Peening on the Microstructure, Tensile and Heat Transport Properties of Alloy D9, Lasers Manuf. Mater. Process., 2020, 7, p 259–277.
[29] J.B. Zhao, J.J. Wu, X.L. Hu, Y. Q. Yang, H.C. Qiao, Effect of Laser Shock Processing on Mechanical Properties of Ti-45.5Al-2Cr-2Nb-0.15B Alloy. Optik, 2020, 217, p 164715.
[30] R. Fabbro, J. Fournier, P. Ballard, D. Devaux and J. Virmont, Physical Study of Laser-Produced Plasma in Confined Geometry, J. Appl. Phys., 1990, 68(2), p 775–784.
[31] J.N. Johnson, Dynamic Deformation Twinning in Shock-Loaded Iron, J. Appl. Phys., 1971, 42(11), p 4171–4182.
[32] Y. D. Im, Y. K. Lee, H. K. Park, K. H. Song, Effect of the Initial Grain Size and Orientation on the Formation of Deformation Twins in Ti-15Mo alloy. J. Mater. Sci., 2017, 52(19), p 11668–11674.
[33] Y.G. Liu, M.Q. Li and H.J. Liu, Surface Nanocrystallization and Gradient

Structure Developed in the Bulk TC4 Alloy Processed by Shot Peening, J. Alloy. Compd., 2016, 685, p 186–193.
[34] J.J. Wu, J.B. Zhao, H.C. Qiao, Y. Lu, B.Y. Yu, T.Y. Hu and Y.N. Zhang, The Application Status and Development of Laser Shock Processing, Opto-Electron. Eng., 2018, 45(02), p 6–12.
[35] Y.L. Wu, Y. Xiong, W. Liu, Z.G. Chen, X. Zhang, S.B. Wang and W. Cao, Effect of Supersonic Fine Particle Bombardment on Microstructure and Fatigue Properties of Ti-6.5Al-3.5Mo-1.5Zr-0.3Si Titanium Alloy at Different Temperatures, Surf. Coat. Tech., 2021, 421, p 127473.
[36] X.D. Ren, Y.K. Zhang, H.F. Yongzhuo, L. Ruan, D.W. Jiang, T. Zhang and K.M. Chen, Effect of Laser Shock Processing on the Fatigue Crack Initiation and Propagation of 7050–T7451 Aluminum Alloy, Mater. Sci. Eng. A, 2018, 528(6), p 2899–2903.
[37] C. Ye, A. Telang, A.S. Gill, S. Suslov, Y. Idell, K. Zweiacker, J.M.K. Wiezorek, Z. Zhou, D. Qian, S.R. Mannava and V.K. Vasudevan, Gradient Nanostructure and Residual Stresses Induced by Ultrasonic Nano-Crystal Surface Modification in 304 Austenitic Stainless Steel for High Strength and High Ductility, Mater. Sci. Eng. A, 2014, 613, p 274–288.
[38] H. Liu, J.J. Yang, X.Y. Zhao, Y.Y. Sheng, W. Li, C.L. Chang, Q. Zhang, Z.T. Yu and X.J. Wang, Microstructure, Mechanical Properties and Corrosion Behaviors of Biomedical Ti-Zr-Mo-xMn Alloys for Dental Application, Corros. Sci., 2019, 161, p 108195.
[39] U. Trdan and J. Grum, Evaluation of Corrosion Resistance of AA6082-T651 Aluminium Alloy After Laser Shock Peening by Means of Cyclic Polarisation and ElS Methods, Corros. Sci., 2012, 59, p 324–333.
[40] S.R. Kumar, K. Gudimetla, P. Venkatachalam and B. Ravisankar, Stress Corrosion Cracking of Al7075 Alloy Processed by Equal Channel Angular Pressing, Int. J. Eng. Sci. Technol., 2010, 2(12), p 53–61.
[41] Z.H. Deng, Q.B. Liu, P. Xu and Z.H. Yao, Corrosion Resistance and Mechanism of Metallic Surface Processed by Square-Spot Laser Shock Peening, J. Mater. Eng., 2018, 46(08), p 140–147.
[42] X.C. Li and Y.K. Zhang, Effect of Laser Shock Times on Electrochemical Performance of AZ31 Magnesium Alloy, Laser Technol., 2015, 39(04), p 466–470.
[43] M. Levy and G.N. Sklover, Anodic Polarization of Titanium and Titanium Alloys in Hydrochloric Acid, J. Electrochem. Soc., 1969, 116(3), p 323–328.
[44] Y. Yang, W.F. Zhou, Z.P. Tong, L. Chen, X.Y. Yang, E.A. Larson and X.D. Ren, Electrochemical Corrosion Behavior of 5083 Aluminum Alloy Subjected to Laser Shock Peening, J. Mater. Eng. Perform., 2019, 28(10), p 1–11.